Reviewer #1

We sincerely thank you for your recognition of our research and for the time and effort devoted to the careful and thorough review of our manuscript (EGUSPHERE-2026-5610). Your constructive comments and suggestions are valuable for improving the scientific analysis, interpretation of the observational results, and overall quality of the manuscript.

We have carefully considered and addressed each of your comments. In response, we have undertaken the following work:

1) Re-examined the interpretation of the lidar polarization measurements, particularly the 532 nm volume depolarization ratio, and expanded the discussion of horizontally oriented ice crystals and the potential seeder–feeder mechanism.

2) Conducted additional quantitative analyses of hydrometeor radar scattering, terminal fall velocity, and Doppler spectral characteristics during the transition from ice cloud to mixed-phase cloud and the subsequent cloud-to-precipitation transition, supported by additional figures and tables.

3) Re-examined the definition and interpretation of the Hydrometeor Sedimentation Index (HSI), assessed its relationship with the radar reflectivity factor (Z_e) and the high-velocity spectral energy fraction (F_{fast}), and performed reflectivity-normalization sensitivity analyses.

4) Further examined the synoptic environment associated with this event and improved the presentation and descriptions of the relevant figures.

Below, we provide point-by-point responses to your comments, together with the corresponding analysis results and observational evidence. The relevant changes will be incorporated into the revised manuscript. We sincerely appreciate your constructive comments and suggestions.

Review report of Manuscript (egusphere-2026-5610) entitled "Continuous Remote Sensing Observations of Hydrometeor Sedimentation Evolution during the Transition from Ice Cloud to Precipitating Mixed-Phase Cloud" by Yuan et al.

General Comments:

This manuscript presents a well-structured observational study on the transition of a cloud system from a high-level ice cloud to a stratiform mixed-phase cloud, ultimately producing short-lived light precipitation. By combining a millimeter-wave cloud radar, multiwavelength polarization lidar, microwave radiometer, and radiosondes, the authors provide a continuous remote sensing perspective on hydrometeor sedimentation evolution. The introduction of the high-velocity spectral energy fraction (F_{fast}) and the Hydrometeor Sedimentation Index (HSI) is an interesting approach that provides a process-oriented framework for characterizing the ice-to-mixed-to-precipitation transition. The dataset is valuable, and the analytical methodology is generally sound.

The manuscript is well within the scope of ACP. To further strengthen the physical depth of the discussion and improve the clarity of the observational evidence, I recommend a **Minor Revision** by addressing some points as listed below, which are expected to make the work more complete and convincing.

Major Comments:

1. In Figure 3, between approximately 23:30 on the first day and 05:00 the next morning, there is a noticeable increase in lidar backscatter accompanied by a sharp decrease in volume depolarization ratio. This feature strongly resembles the optical signature of horizontally oriented ice crystals (Please see Wu et al., 2025, doi: 10.5194/amt-18-3611-2025; He et al., 2021, doi: 10.1016/j.jqsrt.2021.10762), when the outgoing laser is vertically pointed. Another supporting piece of evidence is that lidar signals typically cannot penetrate a liquid water cloud that is thicker than 500 m. Additionally, the temperature around -20 °C is also a well-known favorable environment for the occurrence of horizontally oriented ice crystals (Wu et al., 2026, doi: 10.5194/acp-26-11491-2026). To allow readers to properly evaluate this possibility, could the authors explicitly provide the zenith angle of the lidar beam in the manuscript? If the lidar is pointing strictly vertically, the presence of horizontally oriented ice crystals is highly likely and should be discussed in the context of the observed rather-low depolarization.

Response:

Thank you for pointing out that the enhanced lidar backscatter and low volume depolarization ratio observed in Fig. 3 may be associated with horizontally oriented ice crystals. **The multiwavelength polarization lidar used in this study was vertically pointing, with a zenith angle of 0°.** Under this observational configuration, **specular reflection from horizontally oriented ice crystals can produce enhanced backscatter and a low volume depolarization ratio**. We therefore agree with your interpretation and will expand the discussion in the revised manuscript to address the possible contribution of horizontally oriented ice crystals to the observed lidar optical signatures during this period.

Following your suggestion, we further selected four representative times (23:15, 00:30, 02:30, and 04:30 CST) and jointly examined the vertical profiles of the 1064 nm range-squared-corrected signal (RSCS), the 532 nm volume depolarization ratio, and the corresponding radar reflectivity factor (Z_e) and hydrometeor terminal fall velocity (V_t) from the millimeter-wave cloud radar (MMCR) (new Fig. S3). **The results show that, at certain altitudes, enhanced RSCS coincided with a relatively low volume depolarization ratio, consistent with the optical signatures expected from horizontally oriented ice crystals.** Considering the studies you recommended and the temperature conditions near these altitudes, we suggest that **horizontally oriented ice crystals may have contributed substantially to the observed low depolarization ratios.**

We have also reconsidered the interpretation of this optical feature in the cloud-phase analysis presented in the original manuscript. As shown in Fig. 3, the cloud system progressively extended toward lower altitudes after 23:00 CST, accompanied by enhanced radar echoes and changes in hydrometeor sedimentation characteristics observed by the millimeter-wave cloud radar. Meanwhile, microwave radiometer observations showed persistent liquid water path (LWP) signals, and radiosonde measurements provided the corresponding subfreezing thermodynamic background. **Therefore, our interpretation of the mixed-phase cloud evolution is based on these combined observations, rather than attributing localized low depolarization ratios directly to the presence of supercooled liquid water.** Regarding the lidar penetration characteristics mentioned in your comment, we will also consider the influence of cloud optical attenuation in the revised interpretation.

In response to your comment, **we will explicitly specify the lidar zenith angle in Sect. 2.1 of the revised manuscript and expand the discussion of the possible optical contributions of horizontally oriented ice crystals** in the relevant results associated with Fig. 3 and in the Discussion, citing the studies you recommended. We will also **revise the interpretation of the relationship between low depolarization ratios and cloud phase in Sect. 3.3** to ensure consistency with the observed evolution of hydrometeor radar scattering and sedimentation characteristics revealed by the MMCR.

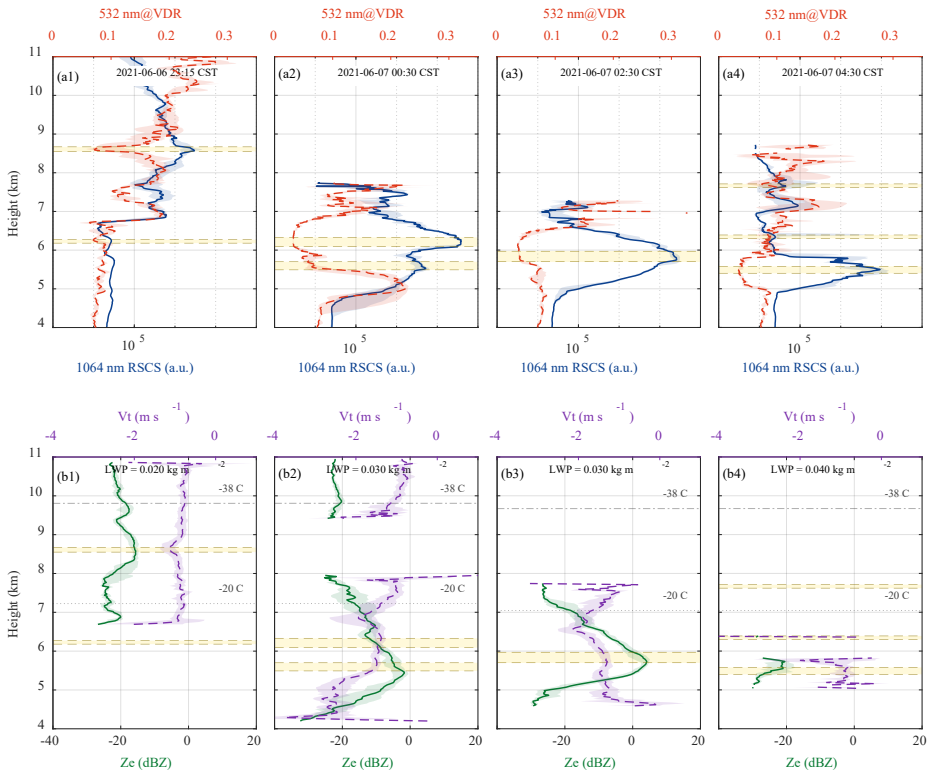


Figure S3. Vertical profiles of lidar and millimeter-wave cloud radar measurements at four representative times on 6–7 June 2021. (a1–a4) The 1064 nm range-squared-corrected signal (RSCS; blue solid lines) and 532 nm volume depolarization ratio (red dashed lines) at 23:15, 00:30, 02:30, and 04:30 CST, respectively. (b1–b4) Corresponding radar reflectivity factor (Ze; green solid lines) and hydrometeor terminal fall velocity (Vt; purple dashed lines), with negative velocities indicating downward sedimentation. Profiles show medians within ±5 min of each time, with shading indicating the 25th–75th percentile ranges. Light-yellow bands mark candidate optical layers with enhanced RSCS and low depolarization ratios. Horizontal dashed lines indicate the reference heights of the −20 °C and −38 °C isotherms derived from the nearest radiosonde profiles. The corresponding liquid water path (LWP) is annotated in each panel.

2. In Figure 3a, during the period from 00:30 to 03:00, there appears to be a classic thin supercooled liquid water layer at ~7 km altitude (and occasionally visible at other heights and times). This suggests that a seeder-feeder process, in which upper ice crystals fall and seed the mid-level liquid water cloud, may be involved in this event. It would be valuable to discuss the potential impact of the seeder-feeder mechanism, as it can be a key process in the formation of stratiform precipitation.

Response:

We thank you for suggesting that the thin layer near 7 km may be associated with the seeder–feeder mechanism. **We agree that sedimenting ice hydrometeors from upper levels may undergo further microphysical growth after entering mid-level cloud layers containing liquid water. The seeder–feeder mechanism therefore provides a plausible explanation for the continued evolution of ice hydrometeors in this mixed-phase cloud.**

As shown in Fig. 3 of the original manuscript, the high-level ice cloud was mainly located at approximately 8–12 km during 19:00–23:00 CST. After 23:00 CST, the radar echoes progressively extended toward lower altitudes, and the main cloud layer developed downward to approximately 5–7 km by 00:30 CST. **During 00:30–03:00 CST, the lidar detected a thin layer of enhanced optical signals near 7 km, while the**

microwave radiometer observations indicated the persistent presence of LWP. Figures 6–7 further show that the downward development of the cloud was accompanied by enhanced Z_e, a shift in V_t toward more negative values, and Doppler spectral broadening. **These observations are consistent with the continued growth and evolution of sedimenting ice hydrometeors after entering the mid-level cloud and provide observational support for discussing the potential role of the seeder–feeder mechanism.**

Meanwhile, considering your first comment regarding horizontally oriented ice crystals, the enhanced backscatter and low volume depolarization ratio near 7 km may also be influenced by specular reflection from ice crystals. **Therefore, the presence of a supercooled liquid water layer cannot be established solely from these optical signatures.** In addition, the thin layer near 7 km was mainly observed during 00:30–03:00 CST, whereas short-lived light surface precipitation occurred at approximately 08:05 CST. As shown in Figs. 8–11 of the original manuscript, fast-sedimenting spectral components became more pronounced after 06:00 CST. **Near 08:00 CST, stronger radar scattering and increased contributions from fast-sedimenting spectral components occurred concurrently and progressively extended toward lower altitudes, showing a closer temporal correspondence with the occurrence of light surface precipitation.**

Following your suggestion, **we will expand the Discussion in the revised manuscript to address the potential role of the seeder–feeder mechanism.** Based on the observed changes in radar scattering and hydrometeor sedimentation, we will discuss the possible further growth of ice hydrometeors after entering the mid-level cloud. We will also **retain the original analysis of the late-stage enhancement of fast-sedimenting spectral components and their downward extension** to explain the observed evolution of the mixed-phase cloud toward short-lived light surface precipitation.

3. In some parts of the analysis, the discussion seems to rely on qualitative descriptions (Section 3). The authors have derived many quantitative parameters from the lidar and radar data (e.g., extinction, backscatter, radar reflectivity, Doppler velocity, spectral width, and so on). Where possible, establishing quantitative relationships between detected/derived parameters and cloud microphysical properties would make the analysis more robust and insightful.

Response:

Thank you for your suggestion to strengthen the quantitative analysis in Sect. 3. In response to your comment**, we have conducted additional statistical analyses of the Z_e, V_t, and Doppler spectral parameters** during two processes examined in the original manuscript: the transition from ice cloud to mixed-phase cloud (23:00–00:30 CST, Figs. 6–7) and the subsequent persistent mixed-phase cloud stage leading to the occurrence of light surface precipitation (00:30–08:30 CST, Figs. 8–11). **The additional results are presented in Fig. S4 and Table S4** to further quantify the evolution of hydrometeor radar scattering and sedimentation characteristics.

During the mixed-phase transition stage, the two-dimensional Z_e–V_t distributions in Fig. 7 of the original manuscript show that hydrometeors characterized by stronger radar scattering and larger terminal fall velocities became increasingly prevalent as the cloud developed downward. The additional statistics further show that, across three consecutive 30 min periods (T1–T3), **the median Z_e increased from −17.70 to −9.07 dBZ, while**

the median $|V_t|$ increased from 0.966 to 1.408 m/s. Meanwhile, **the fraction of valid samples simultaneously satisfying $Z_e \geq -6.40$ dBZ and $|V_t| \geq 1.49$ m/s increased from 0.4% to 27.9%.** These results provide quantitative support for the enhanced radar scattering and hydrometeor sedimentation observed in Figs. 6–7 during the downward development of the high-level ice hydrometeors.

During the persistent mixed-phase cloud stage, Figs. 8–10 of the original manuscript show that, although the main cloud layer remained at approximately 5–7 km for an extended period, the radar scattering and Doppler spectral characteristics continued to evolve. **After 06:00 CST, fast-sedimenting spectral components became more pronounced and progressively extended toward lower altitudes.** To further quantify these changes, we compared valid radar samples within the common altitude range of 5.01–6.99 km between the earlier period (00:30–05:30 CST) and the later pre-precipitation period (06:00–08:00 CST). The results show that **the median Ze increased from −9.693 to −0.578 dBZ, $|V_t|$ from 1.394 to 1.779 m/s, Doppler spectral width (SW) from 0.230 to 0.286 m/s, and the high-velocity spectral energy fraction (F_{fast}) from 0.083 to 0.186.** These quantitative changes are consistent with the enhanced radar scattering, broadening of hydrometeor velocity distributions, and increasing contributions from fast-sedimenting spectral components described in the original manuscript. They also correspond to the late-stage enhancement and downward extension of regions with elevated HSI shown in Fig. 11.

Following your suggestion, **we will incorporate these quantitative results into Sects. 3.3–3.5 of the revised manuscript** and further discuss the evolution of hydrometeor growth and sedimentation in the Discussion, based on the observed changes in radar scattering, terminal fall velocity, and Doppler spectral characteristics. The additional analyses quantify the scattering and sedimentation changes already identified in the original manuscript and further clarify their relationship with the cloud-to-precipitation transition observed in this event.

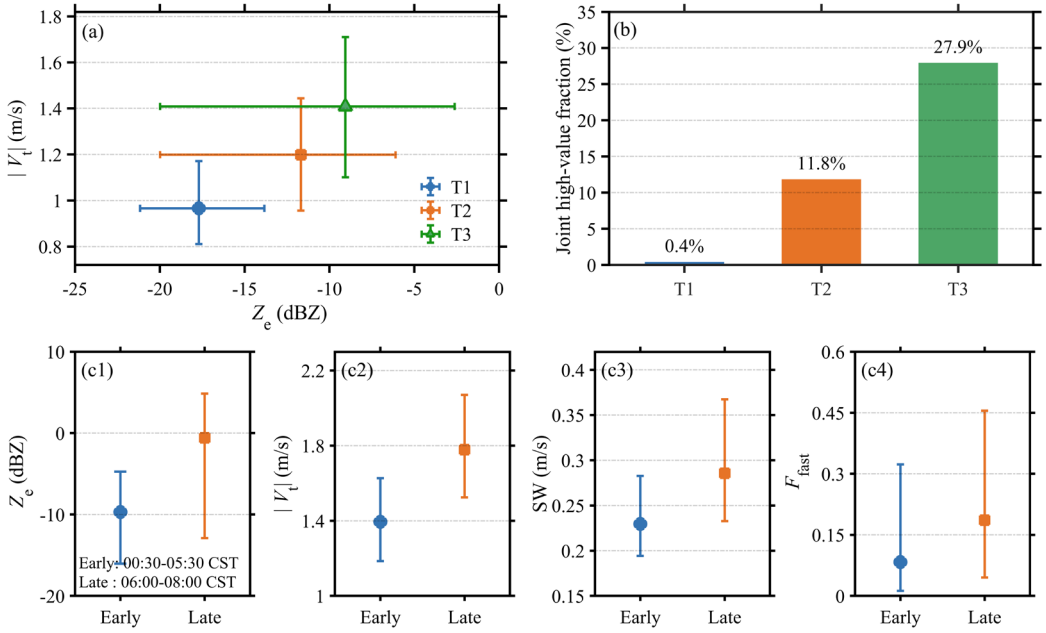


Figure S4. Quantitative changes in radar scattering and hydrometeor sedimentation characteristics during mixed-phase cloud evolution. (a) Medians and interquartile ranges of Z_e and $|V_t|$ during three consecutive 30 min periods of the mixed-phase transition stage (T1: 23:00–23:30; T2: 23:30–00:00; T3: 00:00–00:30 CST). (b) Fractions of valid samples simultaneously satisfying $Z_e \geq -6.40$ dBZ and $|V_t| \geq 1.49$ m/s. (c1–c4) Z_e, $|V_t|$, SW, and F_{fast} within 5.01–6.99 km during the earlier (Early: 00:30–05:30 CST) and later pre-precipitation (Late: 06:00–08:00 CST) periods of the persistent mixed-phase cloud stage. Symbols indicate medians, and error bars represent the 25th–75th percentile ranges.

Table S4. Radar statistics during the mixed-phase cloud transition and before surface precipitation.

(a) Three 30 min windows within the mixed-phase transition stage

Stage (CST)	Valid cells (n)	Z_e (dBZ) median [Q25, Q75]	$\|V_t\|$ (m/s) median [Q25, Q75]	Joint-high (%)
T1 (23:00–23:30)	38,722	–17.70 [–21.16, –13.84]	0.966 [0.811, 1.171]	0.4
T2 (23:30–00:00)	55,189	–11.68 [–19.98, –6.11]	1.199 [0.956, 1.444]	11.8
T3 (00:00–00:30)	52,584	–9.07 [–19.98, –2.62]	1.408 [1.101, 1.711]	27.9

(b) Pre-precipitation comparison (5.01–6.99 km)

Variable	Early (00:30–05:30) median [Q25, Q75]	Late (06:00–08:00) median [Q25, Q75]	Δ median
Z_e (dBZ)	–9.693 [–16.035, –4.722]	–0.578 [–12.894, 4.857]	+9.115
$\|V_t\|$ (m/s)	1.394 [1.191, 1.627]	1.779 [1.524, 2.070]	+0.385
SW (m/s)	0.230 [0.194, 0.283]	0.286 [0.233, 0.367]	+0.056
F_{fast}	0.083 [0.012, 0.323]	0.186 [0.045, 0.455]	+0.103

Note. All times are CST (6–7 June 2021). Values are medians [Q25, Q75] of valid radar time–height cells. T1–T3 are three consecutive 30 min windows within the mixed-phase transition stage (23:00–00:30 CST); n counts cells with valid paired Z_e and V_t measurements, not individual radar range gates. Early and Late-pre are two windows within the persistent mixed-phase cloud stage (00:30–08:30 CST). Joint-high: $Z_e \geq -6.40$ dBZ and $|V_t| \geq 1.49$ m/s. Part (a) uses all occupied radar gates; part (b) uses 5.01–6.99 km (Early: n = 133,927, 55.5% coverage; Late: n = 94,838, 98.3%).

4. Regarding the final stage where measurable precipitation is produced at the ground, could the authors provide an analysis of the possible factors that allowed this stratiform mixed-phase cloud to generate hydrometeors large enough to reach the ground? Specifically, what were the dominant growth mechanisms (e.g., aggregation, riming, or the seeder-feeder effect…) that enabled the particles to grow sufficiently large to overcome updrafts and evaporation below the cloud base? A discussion of this would nicely close the loop on the cloud-to-precipitation transition topic of this work.

Response:

We thank you for suggesting a further analysis of the possible factors that allowed this mixed-phase cloud to produce light surface precipitation, particularly the roles of ice-particle growth, updrafts, and evaporation below the cloud base. Following your suggestion, **we further examined the net downward motion of hydrometeors, the development of low-level radar echoes, and the humidity conditions below the cloud base,** building on the analyses presented in Figs. 8–11 of the original manuscript. **The additional quantitative results are presented in Fig. S5 and Table S5.**

A notable feature of this event is that **the mixed-phase cloud persisted for nearly 8 h after 00:30 CST, during which the microwave radiometer continuously detected LWP, whereas short-lived light surface precipitation occurred only at approximately 08:05 CST.** Figures 6–7 of the original manuscript show that, as ice hydrometeors from upper levels developed downward, the Z_e increased, the V_t shifted toward more negative values, and the Doppler spectra broadened. These changes are consistent with continued growth of ice hydrometeors in the mixed-phase environment. Considering the potential seeder–feeder mechanism raised in your second comment, aggregation, vapor deposition, and possible collection of supercooled liquid droplets may have contributed to this process. **However, the presence of liquid water and sedimenting ice hydrometeors during the earlier period did not coincide with surface precipitation,** highlighting the need to examine the subsequent evolution of hydrometeor sedimentation.

The additional results in Fig. S5 and Table S5 show that, during 07:30–08:05 CST, prior to the occurrence of light surface precipitation, **the median retrieved vertical air velocity (w), downward hydrometeor fall-speed component (F_{down}), and net downward velocity (D_{net}) within 5–7 km were 0.858, 1.900, and 1.043 m/s, respectively. Approximately 95.81% of valid radar time–height sampling cells exhibited net downward motion.** These results indicate that, despite the presence of updrafts, hydrometeors in most valid sampling cells continued to exhibit net downward motion. Further analysis showed that persistent radar echoes were first detected at or below 3, 2, and 1 km at 07:58:40, 07:59:45, and 08:00:40 CST, respectively, showing a close temporal correspondence with the short-lived light surface precipitation observed at approximately 08:05 CST. In addition, the radiosonde profile at 07:15 CST showed relatively low relative humidity in the lower atmosphere beneath the cloud, indicating that descending hydrometeors may have been subject to evaporation or sublimation.

These additional results further complement the late-stage evolution of hydrometeor sedimentation described in Figs. 9–11 of the original manuscript. As shown in those figures, fast-sedimenting spectral components became more pronounced after 06:00 CST. **Near 08:00 CST, stronger radar scattering and increased contributions from fast-sedimenting spectral components occurred concurrently, accompanied by a downward extension of regions with elevated HSI.** Together with the additional evidence of net downward motion and persistent low-level radar echoes, **these observations suggest that the occurrence of light surface precipitation in this event was associated not only with possible continued ice-particle growth in the mixed-phase environment, but also with the late-stage enhancement of fast-sedimenting spectral components and the downward development of radar echoes toward near-surface levels**. Following your suggestion, we will expand the Discussion in the revised manuscript to address the possible ice-particle growth processes, the influence of in-cloud vertical air motion, and the humidity conditions below the cloud base in relation to the observed cloud-to-precipitation transition.

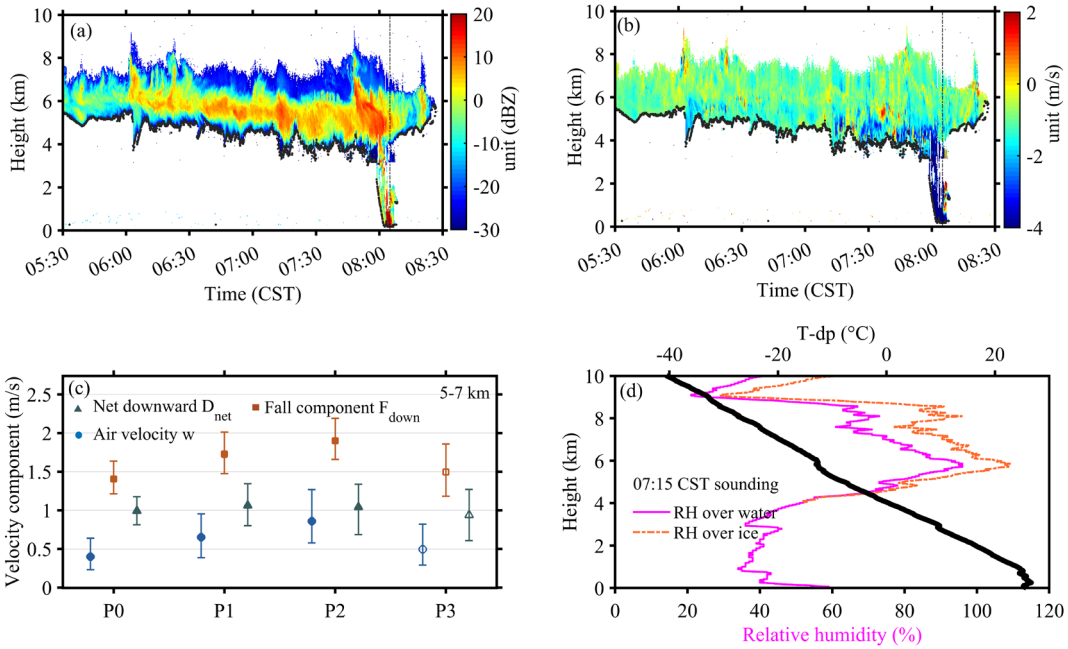


Figure S5. Hydrometeor motion, low-level radar echoes, and humidity conditions before and during the occurrence of light surface precipitation on 7 June 2021. (a, b) Height–time distributions of Z_e and Doppler velocity (V_r) from the millimeter-wave cloud radar during 05:30–08:30 CST. Negative Vr indicates downward motion. Black curves denote the lower radar-echo boundary, and vertical dash-dotted lines mark the approximate time of light surface precipitation (08:05 CST). (c) Vertical air velocity (w), downward hydrometeor fall-speed component (F_{down}), and net downward velocity (D_{net}) within 5–7 km during four periods (P0: 05:30–06:00; P1: 06:00–07:30; P2: 07:30–08:05; P3: 08:05–08:30 CST). Symbols and error bars indicate medians and 25th–75th percentile ranges, respectively. Positive w denotes upward air motion, whereas positive F_{down} and D_{net} denote downward motion.

Table S5. Vertical-motion components within 5–7 km on 7 June 2021.

Stage	Time (CST)	w (m/s)	F_{down} (m/s)	D_{net} (m/s)	Net down (%)	Coverage (%)
P0	05:30–06:00	0.399 [0.230, 0.641]	1.406 [1.215, 1.638]	0.993 [0.814, 1.176]	99.81	89.75
P1	06:00–07:30	0.653 [0.387, 0.955]	1.728 [1.476, 2.011]	1.065 [0.802, 1.345]	99.03	98.74
P2	07:30–08:05	0.858 [0.580, 1.269]	1.900 [1.660, 2.190]	1.043 [0.686, 1.339]	95.81	99.72
P3	08:05–08:30	0.496 [0.290, 0.822]	1.496 [1.182, 1.857]	0.939 [0.608, 1.270]	94.72	63.85

Note. Velocity values are medians [Q25, Q75] of valid radar time–height cells. Net down (%) indicates the percentage of valid cells with $D_{net} > 0$, and Coverage (%) denotes the valid-cell fraction in each period. w is positive upward, whereas $F_{down} = -V_t$ and $D_{net} = -V_r$ are positive downward. P2 and P3 are separated at the approximate time of surface precipitation (08:05 CST) reported in the manuscript.

Minor Comments:

- Section 2.4.2: According to the definition of Eq. (2) in the manuscript, HSI mainly repeats the variation of reflectivity. HSI multiplies Zlin by Ffast, and Ffast is a fraction between 0 and 1, but Zlin can range from 0.001(-20 dBz as Ze) to 100 (20 dBz as Ze). HSI is therefore dominated by Zlin, and its increase mainly repeats the reflectivity increase. What about considering normalizing Ze before multiplying, over the observed range or as a percentile, so that both factors carry comparable weight? A direct comparison of HSI with Ze alone would also show what the index adds.

Response:

Thank you for pointing out that the dynamic range of the linear radar reflectivity factor may influence HSI. We agree that the relative contributions of radar reflectivity and the high-velocity spectral energy fraction to variations in HSI need to be further examined. Following your suggestion, **we conducted a comparison of the original HSI, the linear radar reflectivity factor (Z_{lin}), and the high-velocity spectral energy fraction (F_{fast}) using the same set of valid samples.** We further examined the sensitivity to two reflectivity-normalization approaches: normalization with clipping based on a predefined dBZ range (N1) and normalization based on the percentile rank of dBZ values (N2). **The above comparisons and normalization sensitivity analyses are summarized in the new Fig. S6,** which provides a direct comparison of the spatiotemporal variations in Z_{lin}, F_{fast}, and the original HSI, as well as the effects of different reflectivity-normalization approaches on the vertically integrated HSI evolution.

Among 386,583 common valid radar time–height sampling cells, **the original HSI was highly correlated with Z_{lin}, with a Pearson correlation coefficient of 0.972 and a Spearman rank correlation coefficient of 0.756.** Both variables increased markedly during the later part of the observation period, indicating that changes in linear reflectivity had a substantial influence on the original HSI. Meanwhile, F_{fast} did not vary entirely in parallel with Z_{lin}. During some earlier periods, F_{fast} already had a considerable contribution, but the corresponding HSI remained relatively low because the overall radar scattering was weak. This indicates that **F_{fast} modulates the variation in HSI, although HSI is not an observational parameter independent of radar reflectivity.** The corresponding height-time distributions and integrated comparisons are presented in Fig. S6 (a-d).

The two normalization approaches (N1 and N2) produced broadly similar spatiotemporal distributions, both retaining the enhanced signals and their downward extension during the later stage. However, compared with the original HSI, **the normalized 30 min vertically integrated time series differed in their relative variations and the timing of their peaks.** This indicates that reflectivity normalization affects the relative temporal characteristics of HSI, and that the normalized results are not fully equivalent to the original HSI. The comparison of the original HSI and the two normalization approaches is shown in Fig. S6 (e).

Based on these results and your suggestion, we retain the original definition of HSI in Eq. (2), $HSI = \mathrm{Zlin} \times F_{fast}$. This index is intended to characterize the radar scattering contribution associated with fast-sedimenting spectral components by jointly accounting for their relative spectral energy contribution and the corresponding overall radar scattering intensity, rather than to construct a precipitation-prediction index independent of Z_e. We

will further clarify the physical meaning of HSI in Sect. 2.4.2 of the revised manuscript and explain its role in the cloud-to-precipitation transition examined in this event in Sect. 3.5, with reference to the variations in Ze and F_{fast}.

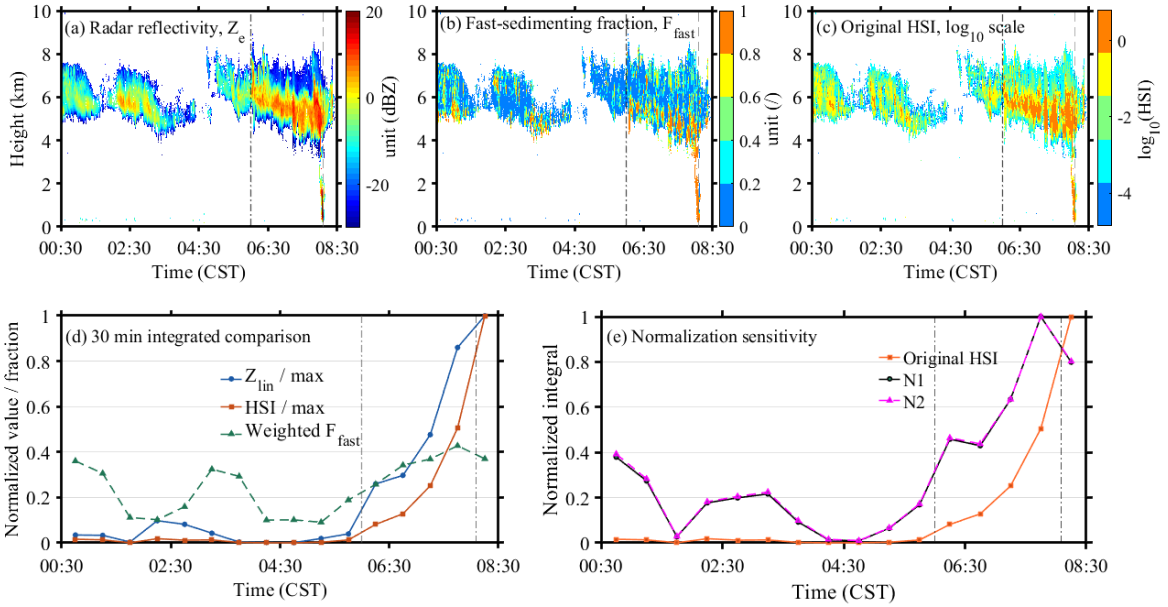


Figure S6. Comparison of radar reflectivity, fast-sedimenting spectral contributions, and HSI, together with reflectivity-normalization sensitivity analyses during the persistent mixed-phase cloud stage. (a–c) Height–time distributions of the Z_e, F_{fast}, and original HSI (log_{10} scale), respectively, from 00:30 to 08:30 CST on 7 June 2021. (d) Maximum-normalized 30 min vertical integrals of the Z_{lin} and HSI, together with the F_{fast}. (e) Comparison of the 30 min vertically integrated time series of the original HSI and two reflectivity-normalization approaches: N1, normalization with clipping based on a predefined dBZ range; and N2, normalization based on the percentile rank of dBZ values. Each series is normalized by its own maximum. The vertical dotted and dashed lines indicate 06:00 CST and approximately 08:05 CST, respectively.

- Section 2.4.2: HSIint is mathematically constrained to increase with radar echo depth, which deepened by ~3 km during this event (valid echo boundaries zb to zt are defined in Sect. 2.4.2; the lower boundary descends from 8 km to 5-6 km after 23:00, as noted in Sect. 3.3). Thus, the rise of HSIint is largely an artifact of cloud deepening, regardless of microphysical changes. Although the authors acknowledge this (p7, L22-23), Sects. 3.5 and the conclusions still interpret the HSIint increase as the precursor to precipitation. This logical inconsistency should be resolved to ensure consistency throughout the manuscript.

Response:

Thank you for pointing out that the vertically integrated HSI (HSI_{int}) may be affected by changes in the vertical extent of valid radar echoes. We agree with this observation. According to Eqs. (3) and (4) in the original manuscript, HSI_{int} is calculated by vertically integrating HSI over all range gates containing valid meteorological radar echoes. Therefore, **its value depends not only on the local HSI values at individual heights but also on the number of valid range gates included in the integration.** Following 23:00 CST, the lower boundary of the cloud descended from approximately 8 km to 5–6 km, and **the newly included valid radar echo gates may have contributed to the increase in HSI_{int}.** We therefore recognize the need to distinguish the effects of an expanded integration range from changes

in local HSI values, rather than directly interpreting an increase in HSI_{int} as evidence of enhanced hydrometeor growth or sedimentation.

We further examined the HSI height–time distribution and cloud evolution shown in Fig. 11 of the original manuscript. The cloud underwent pronounced downward development during 23:00–00:30 CST. However, after entering the persistent mixed-phase cloud stage (00:30–08:30 CST), the main cloud layer remained primarily at approximately 5–7 km, without further rapid downward development comparable to that during the preceding transition stage. Meanwhile, local HSI values remained generally low during 01:00–05:30 CST. **After 06:00 CST, regions with elevated HSI became progressively more frequent, mainly in the middle and lower portions of the cloud, and extended further downward (Fig. 11b)**. This height–time distribution indicates that the late-stage evolution of HSI should be examined in terms of its local changes within the cloud, rather than inferred solely from the vertically integrated HSI time series.

Based on this analysis, we agree that the interpretation of HSI_{int} needs to be revised. **In the revised** manuscript, we will clarify that HSI_{int} reflects both the local HSI values and their vertical extent, and will no longer interpret an increase in HSI_{int} alone as a precursor to surface precipitation. In Sects. 3.5 and 5, **we will instead emphasize the enhancement of local HSI values and their downward extension**, as shown in Fig. 11(b), together with the concurrent variations in Z_e and F_{fast}. These observations will be used to describe the late-stage evolution of hydrometeor radar scattering and fast-sedimenting spectral contributions, and their temporal correspondence with the occurrence of short-lived light surface precipitation at approximately 08:05 CST.

- Based on the temporal evolution of the cloud system described in the manuscript, this precipitation event appears to be associated with the passage of a frontal system. Is it possible to provide an analysis of more complete meteorological context regarding this?

Response:

Thank you for pointing out the possible association of this precipitation event with frontal system activity and for suggesting a more comprehensive analysis of the meteorological background. Following your suggestion, we further examined the meteorological conditions around Jinghe station on 6–7 June 2021. **We added an analysis of the spatiotemporal distributions of equivalent potential temperature at 850 hPa, mean sea-level pressure, and relative humidity, vertical motion, and horizontal wind fields at 750 hPa (Fig. S8).**

The analysis includes four representative times: 19:00 and 23:00 CST on 6 June, and 03:00 and 08:00 CST on 7 June. The results show that **Jinghe station remained under a relatively warm and moist low-level thermodynamic environment during the observation period. Moist conditions were also present in the middle troposphere, accompanied by localized upward motion.** These environmental

conditions provided a favorable synoptic-scale background for the maintenance and subsequent evolution of the stratiform mixed-phase cloud.

However, **the equivalent potential temperature, mean sea-level pressure, and wind fields at these four representative times do not show a clear and continuous pattern indicating the direct passage of a front over Jinghe station.** Therefore, we have supplemented the discussion of the synoptic-scale meteorological background and its possible association with regional weather-system activity in the revised manuscript.

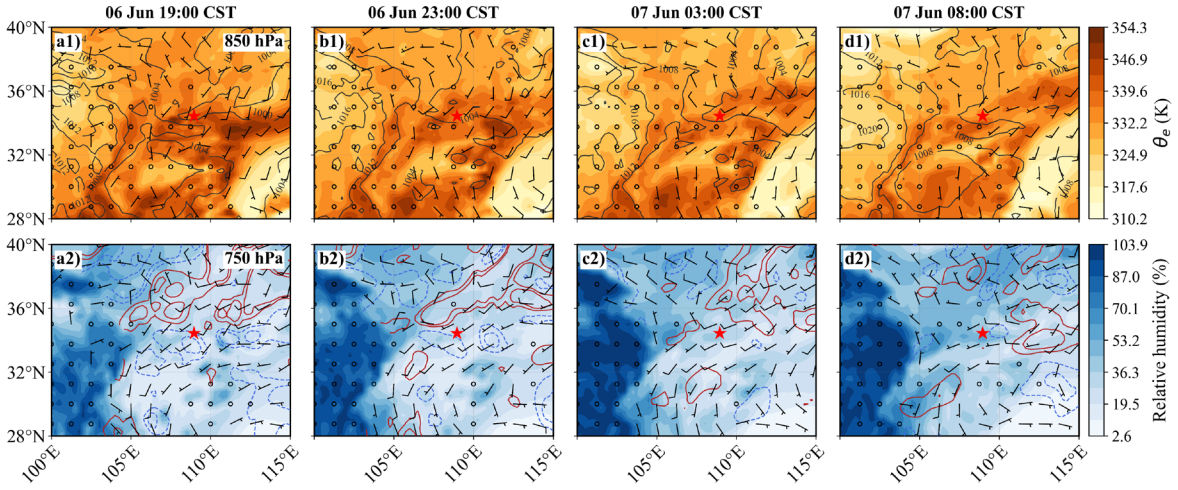


Figure S8. Evolution of the meteorological conditions around Jinghe station on 6–7 June 2021. The four columns correspond to 19:00 and 23:00 CST on 6 June, and 03:00 and 08:00 CST on 7 June, respectively. (a1–d1) Equivalent potential temperature (θ_e; yellow–orange shading), mean sea-level pressure (black contours at 2 hPa intervals), and horizontal wind fields at 850 hPa. (a2–d2) Relative humidity (blue shading), pressure vertical velocity (ω), and horizontal wind fields at 750 hPa. Red solid contours indicate upward motion (ω = −0.2 and −0.4 Pa/s), whereas blue dashed contours indicate downward motion (ω = +0.2 and +0.4 Pa/s). Red stars indicate the location of Jinghe station.

- Figure 3: color bars for Figs 3c and 3d can be changed. Some informations on the right hand of y axis are overlapped. It would be better to add 0 and -38 degree isotherms in Fig 3a.

Response:

Thank you for your specific suggestions regarding the color bars and axis labels in Fig. 3. We have adjusted the color scale for the 532 nm volume depolarization ratio in Fig. 3(c) and revised the presentation of the water-vapor density color scale in Fig. 3(d). We have also rearranged the tick marks and labels of Vint and LWP on the right-hand axes to eliminate the overlap in the original figure.

In addition, reference heights of the 0 °C and −38 °C isotherms have been added to Fig. 3(a), as shown below. Both reference heights were determined from the radiosonde temperature profile measured at 07:15 CST on 7 June 2021. Their source has been specified in the revised figure caption. These horizontal reference lines indicate the corresponding isotherm heights derived from a single radiosonde profile and do not represent the continuous temporal evolution of the isotherms throughout the observation period.

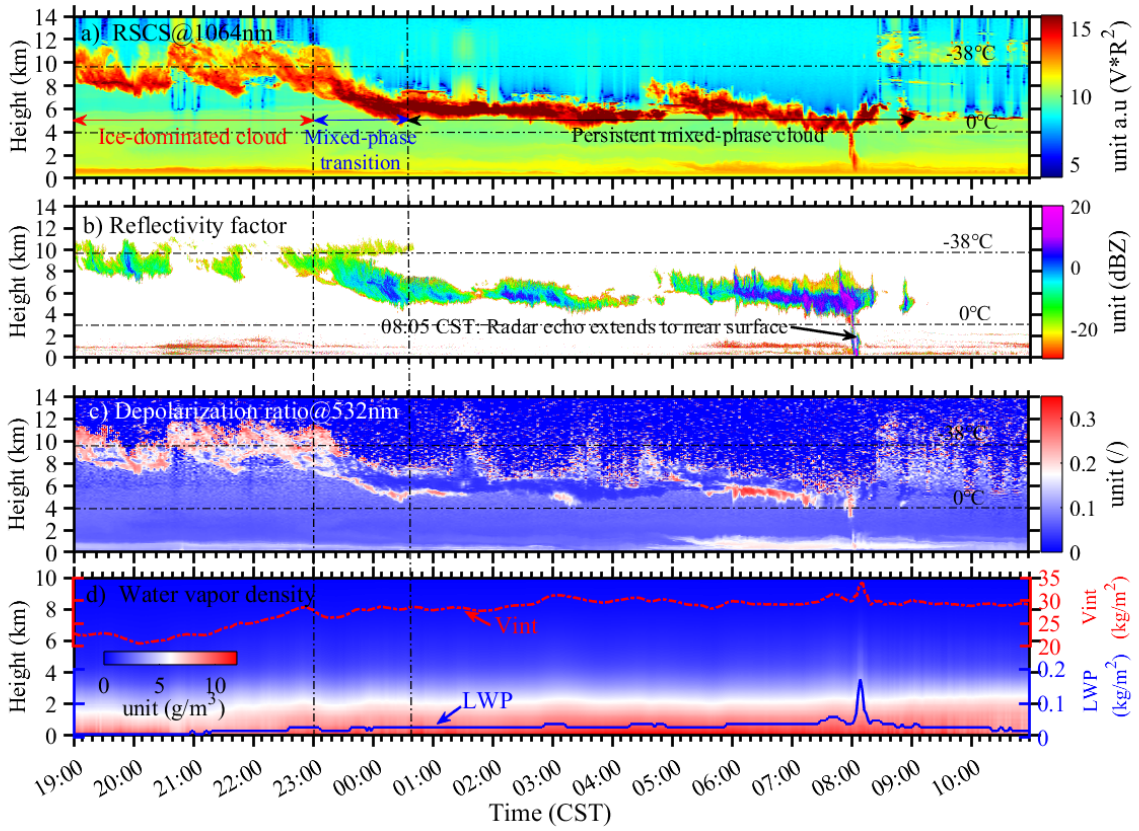


Figure 3. Multi-instrument ground-based remote-sensing observations of the cloud-system evolution on 6–7 June 2021. (a) 1064 nm RSCS from the multiwavelength lidar. (b) Ze from MMCR. (c) 532 nm lidar volume depolarization ratio, with radiosonde temperature profiles at 19:15 and 07:15 CST overlaid; the cyan and black curves indicate the corresponding moist- and dry-adiabatic temperature profiles, respectively. (d) Water-vapor density retrieved by the microwave radiometer, with Vint (red dashed line) and LWP (blue solid line). Vertical dashed lines separate the ice-dominated cloud stage, mixed-phase transition stage, and persistent mixed-phase cloud stage. At approximately 08:05 CST, the radar echo extended toward near-surface levels, coinciding with the occurrence of short-lived light precipitation at the surface. The horizontal dash-dotted lines in (a) indicate the reference heights of the 0 °C and −38 °C isotherms derived from the radiosonde temperature profile at 07:15 CST on 7 June 2021.

- p12 L24, typo: "…more pronounced sedimentatio." → "sedimentation".

Response:

Thank you for pointing out this typographical error. We will correct “sedimentatio” to “sedimentation” in the corresponding sentence in Sect. 3.3 of the revised manuscript.

- Fig. 7b: some colored points outside the axes? In b1-b3 a band of light blue points continues below the lower axis limit of -2.5 m s-1 and outside the frame, over the tick labels and the axis title. Please explain what these points are. Fig. 7b contains red and black crosses, but the caption explains only the black ones.

- **Response:**

Thank you for pointing out the graphical display and marker-description issues in Fig. 7(b1 – b3).

Upon inspection, the light-blue regions represent low-density areas of the normalized two-dimensional joint density distribution of Z_e and V_t, rather than additional data points or a distinct hydrometeor population. In the original figure, these regions are contained within the axes. However, in the preprint PDF, some light-blue regions extend below the lower y-axis limit of −2.5 m/s and overlap

the axis tick labels and title. This may have resulted from an error during PDF conversion. We will re-export the figure and check its appearance in the final submission PDF.

Regarding the red and black crosses, we clarify that both sets of markers were manually selected by the authors to indicate two representative locations within the high-density regions of the Z_e – V_t joint density distributions. They do not represent different statistical methods or quantities. To avoid ambiguity, the two markers have been changed to black crosses in the revised Fig. 7, and their meaning has been clarified in the figure caption. These markers are intended only to indicate representative locations within the high-density regions.

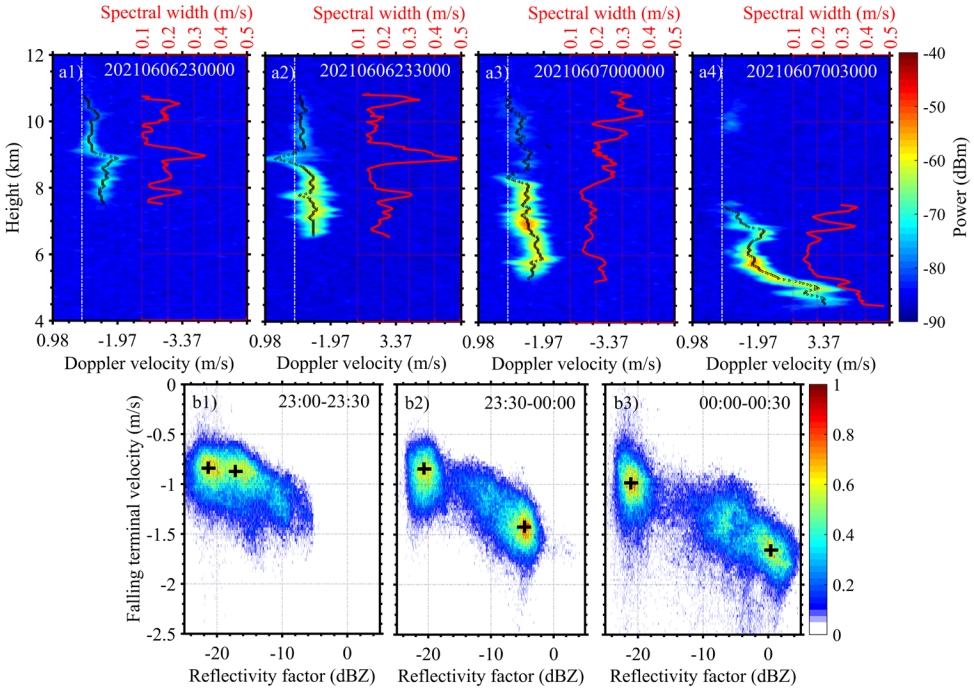


Figure 7. Evolution of Doppler spectra and the Ze–Vt relationship during the mixed-phase transition stage (23:00–00:30 CST). (a1–a4) Vertical profiles of Doppler power spectra at 23:00, 23:30, 00:00, and 00:30 CST, respectively. Colors indicate spectral power, black dotted curves denote the spectral peak velocity at each height, and red curves indicate Doppler spectral width (SW). (b1–b3) Normalized two-dimensional density distributions of Ze and Vt during 23:00–23:30, 23:30–00:00, and 00:00–00:30 CST, respectively. Colors indicate normalized density. The two black crosses in each of (b1–b3) indicate manually selected representative locations in the two high-density regions.